



Electronic properties in intrinsically disordered double perovskites: $\text{Sr}_3\text{MnMo}_2\text{O}_9$ and $\text{Ba}_3\text{MnMo}_2\text{O}_9$ with Mo^{5+} valence state



C.A. López ^{a,*}, M.E. Saleta ^b, J.C. Pedregosa ^a, R.D. Sánchez ^b, D.G. Lamas ^c, J.A. Alonso ^d, M.T. Fernández-Díaz ^e

^a INTEQUI-Area de Química General e Inorgánica “Dr. G.F.Puelles”, Facultad de Química, Bioquímica y Farmacia, Universidad Nacional de San Luis, Chacabuco y Pedermera, 5700 San Luis, Argentina

^b Centro Atómico Bariloche, Comisión Nacional de Energía Atómica and Instituto Balseiro, Universidad Nacional de Cuyo, 8400 S.C. de Bariloche, Río Negro, Argentina

^c CONICET - Escuela de Ciencia y Tecnología, Universidad Nacional de General San Martín, Martín de Irigoyen 3100, Edificio Tornavía, Campus Miguelete, (1650) San Martín, Pcia. de Buenos Aires, Argentina

^d Instituto de Ciencia de Materiales de Madrid, CSIC, Cantoblanco, E-28049, Madrid, Spain

^e Institut Laue-Langevin, B. P. 156, 38042 Grenoble Cedex 9, France

ARTICLE INFO

Article history:

Received 12 September 2015

Received in revised form

19 November 2015

Accepted 25 November 2015

Available online 1 December 2015

Keywords:

Inorganic materials

Crystal structure

Electronic properties

Magnetic measurements

Neutron diffraction

Impedance spectroscopy

ABSTRACT

$\text{Sr}_3\text{MnMo}_2\text{O}_9$ and $\text{Ba}_3\text{MnMo}_2\text{O}_9$ double perovskites with Mo^{5+} valence states have been prepared in polycrystalline form by thermal treatment, in reducing atmosphere (H_2/N_2 flow), of previously decomposed citrate precursors. These materials have been studied by X-ray and neutron powder diffraction (XRPD, NPD), magnetic and transport measurements. At room temperature, the crystal structure of $\text{Sr}_3\text{MnMo}_2\text{O}_9$ is monoclinic, space group $P2_1/n$, with $a = 5.6564(1)$ Å, $b = 5.6383(1)$ Å, $c = 7.9765(2)$ Å, $\beta = 89.994(7)^\circ$; whereas $\text{Ba}_3\text{MnMo}_2\text{O}_9$ presents a cubic lattice, space group $Fm\bar{3}m$, with $a = 8.14900(8)$ Å. These samples present a frustrated magnetic interaction below to 12 and 9 K for $\text{Sr}_3\text{MnMo}_2\text{O}_9$ and $\text{Ba}_3\text{MnMo}_2\text{O}_9$, respectively. Semiconductor behaviour, observed either from d.c. or a.c. measurements, was modelled by a variable-range hopping mechanism. This transport behaviour is in accord with the electronic configurations $\text{Mn}^{2+}(3d^5) - \text{Mo}^{5+}(4d^1)$ and supports the absence of mixed valence states in both double perovskites.

© 2015 Elsevier B.V. All rights reserved.

1. Introduction

Double perovskite oxides with the general formula $\text{A}_2\text{B}'\text{B}''\text{O}_6$ have been the object of extensive research because of their rich variety of physical properties. Double perovskites are currently of significant interest for the development of renewable energy technologies such as solid oxide fuel cells, thermoelectric (TE) modules and high-temperature superconductors [1–6]. The revival of interest in this family was triggered by a report on $\text{Sr}_2\text{FeMoO}_6$ [7], demonstrating that in the electronic structure only minority spins are present at the Fermi level; this material was shown to exhibit intrinsic tunneling-type magnetoresistance (TMR) at room temperature (RT) [7,8].

Despite the large number of double perovskites informed up to

now, few studies are devoted to compounds with stoichiometry $\text{A}_3\text{B}'_2\text{B}''\text{O}_9$. This particular type of stoichiometry is apparently more complex, but these oxides are also double perovskites $\text{A}_2\text{B}'_{1.33}\text{B}''_{0.66}\text{O}_6$ whose crystallographic formula can be re-written as $\text{A}_2[\text{B}']_a[\text{B}''_{1/3}\text{B}''_{2/3}]_b\text{O}_6$, where a and b denote the crystallographic sites in the corresponding space group. Thus, they, display an intrinsic partial disordering over half of the perovskite ($\text{B}'_{1/3}\text{B}''_{2/3}$) positions. Furthermore, this composition offers the possibility of changing the oxidation states of the B' and B'' ions and consequently modifying the electrical and magnetic properties. Some double perovskites have been reported as ferrimagnets with Curie temperatures (T_C), in some cases, above RT. Previously we have prepared and studied the magnetic properties of some double perovskites with $\text{B}' = \text{Fe}$, as $\text{Sr}_3\text{Fe}_2\text{MoO}_9$, $\text{Ca}_3\text{Fe}_2\text{WO}_9$, $\text{Sr}_3\text{Fe}_2\text{UO}_9$ and $\text{Sr}_3\text{Fe}_2\text{TeO}_9$ and observed a ferrimagnetic behaviour below $T_C = 280$ K, $T_C = 310$, $T_C = 330$ K and $T_C = 717$ K, respectively [9–12]. Also, we have induced a semi-metallic behaviour and colossal magnetoresistance (CMR) properties in these compounds, as that

* Corresponding author.

E-mail address: calopez@unsl.edu.ar (C.A. López).

recently reported in $\text{Sr}_3\text{Fe}_2\text{MoO}_9$ via chemical reduction, by topotactical removal of oxygen atoms [13]. In addition, the manganese in this structure led to an interesting charge ordering behaviour, as was reported in $\text{Ca}_3\text{Mn}_2\text{NbO}_9$ [14].

In contrast with the $\text{A}_3\text{B}'_2\text{B}''\text{O}_9$ family (with A: earth alkaline cations; B': firsts transition metal row; B'': second and third transition row or p-block element) we can also define the related $\text{A}_3\text{B}'\text{B}''_2\text{O}_9$ stoichiometry (or $\text{A}_2\text{B}'_{0.66}\text{B}''_{1.33}\text{O}_6$; also intrinsically disordered), which makes it possible to tune different oxidation states for B' and B''. Recently, we have prepared and studied the magnetic and transport properties of $\text{Ba}_3\text{FeMo}_2\text{O}_9$ where the coexistence of localized and itinerant electrons (Fe^{3+} - $\text{Mo}^{4+/5+}$) leads to a non-negligible magnetoresistance properties [15]. These results motivated the interest to obtain and study this system but with Mn cations.

In the present work, we describe the results of fully replacing Fe by Mn in the precedent systems, Mn ions being able to adopt varied oxidation states. We report on the synthesis of $\text{Sr}_3\text{MnMo}_2\text{O}_9$ and $\text{Ba}_3\text{MnMo}_2\text{O}_9$ (hereafter labelled SMM and BMM, respectively) double perovskites obtained by precursor method in reduced conditions (H_2/N_2). The well-crystallized samples were characterized by X-ray and neutron powder diffractions and their crystallographic features structure was refined by the Rietveld method. In order to obtain a better understanding of this new system with Mn/Mo = 0.5 we performed magnetic, d.c. and a.c. electrical transport measurements. Finally, the Mn oxidation state was confirmed by X ray absorption spectroscopy experiments.

2. Experimental

SMM and BMM double perovskites were prepared as black polycrystalline powders from citrate precursors obtained by soft chemistry procedures in controlled atmosphere. Stoichiometric amounts of analytical grade $\text{Sr}(\text{NO}_3)_2$ (or $\text{Ba}(\text{NO}_3)_2$), MnCO_3 , and $(\text{NH}_4)_6\text{Mo}_7\text{O}_{24}\cdot 4\text{H}_2\text{O}$ were dissolved in citric acid. The citrate and nitrate solutions were slowly concentrated, leading to organic resins containing a random distribution of the cations involved at an atomic level. These resins were first dried at 180 °C and then all the organic materials and nitrates were eliminated in a subsequent treatment at 600 °C in air, for 12 h, giving rise to highly reactive precursor materials.

The conditions for the SMM and BMM synthesis were established from several trials under different conditions of temperature and time, in H_2/N_2 (5/95) atmosphere. The optimal conditions resulted from the treatment in H_2/N_2 (5/95) atmosphere at 1200 °C for 12 h. The rate of heating and cooling was 5 °C min^{-1} . Thermal treatments longer than 12 h did not produce changes in the obtained samples, suggesting that the new samples reached equilibrium with the atmosphere before this treatment time. The initial identification and characterization of the samples was carried out by X-ray powder diffraction (XRPD).

The crystallographic study was carried out from XRPD patterns collected at RT. The experimental XRPD patterns were obtained on a diffractometer Rigaku D-MAX-IIIC with $\text{Cu K}\alpha$ ($\lambda = 1.5418$ Å) radiation. The data were collected over a range of 10–120° (2θ) with a step of 0.02°; the effective counting time was 5 s per step.

For the structural refinements, neutron powder diffraction (NPD) pattern was collected at RT in the D2B neutron diffractometer, with $\lambda = 1.594$ Å, belonging to *Institute Laue Langevin* (ILL), Grenoble, France. The patterns were refined by the Rietveld method [16] using the *FullProf* refinement program [17]. A pseudo-Voigt function was chosen to generate the line shape of the diffraction peaks. In the final runs, the following parameters were refined: scale factors for the main and impurity phases, background coefficients, zero-point error, unit cell parameters, pseudo-Voigt

corrected for asymmetry parameters, positional coordinates, anisotropic thermal factors, and antisite disorder of Mn/Mo and occupancy factors for oxygen atoms.

Thermogravimetric analysis was performed in a Shimadzu TG-50H thermal analyzer apparatus using flowing air at 50 mL/min from 25 °C to 1000 °C, at a heating rate of 5 °C/min. About 18 mg of the sample was used in the experiment.

The magnetic measurements were performed in a commercial superconducting quantum interference device (SQUID-Quantum Design MPMS-5S) magnetometer, with fields up to 50 kOe, in the $2 \leq T \leq 300$ K temperature range.

XANES (X-ray absorption near edge structure) studies were performed for the Mn K-edge. These tests were carried out in the D04B - XAFS1-11681 beamline of the Brazilian Synchrotron Light Laboratory (LNLS, Campinas, Brazil). The Mn K-edge absorption spectra were recorded in transmission mode.

The d.c. electrical transport properties were performed with a Keithley multimeter and d.c. current source equipment by the conventional four probe technique. The a.c. measurements were performed in an Agilent 4294A impedance analyzer. In both cases the experiments were carried out between 80 K and 300 K. For these electrical transport experiments, polycrystalline powder was pressed and sintered in the same conditions of the synthesis. For the resistance and impedance measurements the powders were pressed in bar- and disk-shaped pellets respectively and sintered at the same final temperature used in the synthesis.

3. Results

3.1. Crystallographic structure

The XRPD patterns of SMM and BMM (Fig. 1) are characteristic of perovskite structures, cubic for BMM, and showing the splitting of certain high-angle reflections for SMM, typical of a monoclinic symmetry. Minor amounts of BaMoO_3 in BMM were detected from XRPD and NPD data.

The structural refinement was performed from XRPD and NPD data at RT. For BMM, the $Fm\bar{3}m$ space group (No. 225), $Z = 4$, was considered, with unit-cell parameter related to a_0 (ideal cubic perovskite, $a_0 \approx 3.9$ Å) as $a = 2a_0$. Ba atoms were located at $8c$ ($1/4, 1/4, 1/4$) positions and oxygen atoms at $24e$ ($x, 0, 0$) sites. In this space

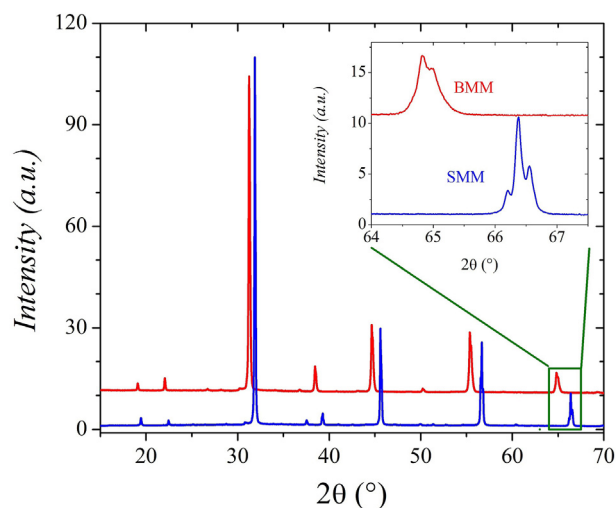


Fig. 1. XRPD patterns with $\text{Cu K}\alpha$ radiation for SMM and BMM. The inset shows the reflections corresponding to the cubic space group $Fm\bar{3}m$ for BMM and the splitting typical of a monoclinic distortion for SMM.

group there are two possible sites for B-type cations, namely, *4a* and *4b*. We placed Mn/Mo at random at *4a* (0,0,0) and *4b* ($\frac{1}{2}, \frac{1}{2}, \frac{1}{2}$) sites, and refined the long-range ordering as described below.

For SMM the structure is defined in the $P2_1/n$ space group, with unit-cell parameters are related to a_0 as $a \approx b \approx \sqrt{2}a_0$ and $c \approx 2a_0$. Sr atoms were located at the $4e$ (x,y,z) positions, and the three kinds of oxygen atoms, O1, O2 and O3 at $4e$ positions. For this space group $P2_1/n$ there are two possible sites for B type cations, namely, $2c$ and $2d$. Mn/Mo were distributed at random at $2c$ ($\frac{1}{2}, 0, \frac{1}{2}$) and at $2d$ ($\frac{1}{2}, 0, 0$) sites, and the long-range ordering between both cations was subsequently refined. The good agreement between the observed and calculated NPD patterns after the refinements is shown in Fig. 2a) and b).

Compounds of formula $A_3B'B''_2O_9$ can be written as $A_2B'_2/3B''_4/3O_6$, following the double perovskite nomenclature. In this case B'/B'' ratio is different than 1. The present compounds $A_3MnMo_2O_9$ show Mn/Mo = 0.5, for which Mn and Mo ions could exhibit the oxidation states $Mn^{2+} - Mo^{5+}$ or alternatively $Mn^{3+} - Mo^{4.5+}$, or all the intermediate situations. In order to obtain a better picture of the distribution of the B cations in the two crystallographic sites and to consider the degree of disorder, we can write the crystallographic formula as $A_2[Mo_{1-\alpha}Mn_\alpha]_{4b}[Mo_{1/3+\alpha}Mn^{2/3-\alpha}]_{4a}O_6$, where $0 \leq \alpha \leq \frac{1}{3}$. Thus, if $\alpha = 0$ we have maximum order (but not full order), and if $\alpha = \frac{1}{3}$ we have maximum disorder. The composition for maximum disorder, i.e. $A_2[Mo_{2/3}Mn^{1/3}]_{4b}[Mo_{1/3}Mn^{2/3}]_{4a}O_6$, corresponds to B cations randomly distributed and $A_2[Mo]_{4b}[Mo_{1/3}Mn^{2/3}]_{4a}O_6$ to maximum order. Based on the preceding discussion, we can define the degree of order (DO) as $DO = 1 - 3\alpha$. For maximum order $DO = 1$ and for random distribution $DO = 0$. DO values are obtained from the refinements of occupancies of B cations in *4a* and *4b* sites (for cubic case).

The most important structural parameters of the crystallographic structure and the discrepancy factors after the refinements are listed in Tables 1 and 2. It can be seen that, within the experimental errors, the Mn/Mo ratio is 0.5 for both phases and the degree orders are 0.89 and 1 for SMM and BMM, respectively. For BMM phase we included $BaMoO_3$ as impurity, defined in the space group $Pm\bar{3}m$ [18]. From the scale factor of the main and secondary phases we estimated the impurity level as wt%: 8.3(2)% of $BaMoO_3$. In both refinements the displacement factors for Mn/Mo atoms were fixed to 0.3 \AA^2 given the opposite signs of the scattering lengths of Mn and Mo, yielding a weak average scattering for both B-sites.

Table 1

Crystallographic parameters for $Sr_3MnMo_2O_9$ phase from NPD data at RT. Space group: $P2_1/n$, $Z = 2$. Unit-cell parameters: $a = 5.6564(1) \text{ \AA}$, $b = 5.6383(1) \text{ \AA}$, $c = 7.9765(2) \text{ \AA}$, $\beta = 89.994(7)^\circ$ and $V = 254.39(1) \text{ \AA}^3$.

a) Positional, displacement and occupancy factors						
Atom	Wyckoff site	x/a	y/b	z/c	$B_{iso}/\text{\AA}^2$	Occ
Sr	4e	0.001(1)	0.007(1)	0.251(2)	0.81(5)	1
Mn	2d	0.5	0	0	0.3*	0.036(6)
Mo	2d	0.5	0	0	0.3*	0.964(6)
Mn	2c	0.5	0	0.5	0.3*	0.632(6)
Mo	2c	0.5	0	0.5	0.3*	0.368(6)
O	4e	0.045(1)	0.498(2)	0.259(2)	0.8(2)	1
O	4e	0.721(2)	0.264(2)	0.024(2)	1.5(4)	1
O	4e	0.241(2)	0.227(2)	0.979(2)	0.9(3)	1

$R_p = 2.06\%$, $R_{wp} = 2.68\%$, $R_{exp} = 5.60\%$, $\chi^2 = 0.23$, $R_{Bragg} = 3.86\%$

b) Main distances (Å) and angles (°)			
[Mn/Mo] $_{2d}O_6$ octahedra		AO $_{12}$ polyhedra	
(Mn/Mo)–O1 (x2)	1.94(2)	Sr–O1	2.88(1)
(Mn/Mo)–O2 (x2)	1.95(1)	Sr–O1	2.78(1)
(Mn/Mo)–O3 (x2)	1.95(1)	Sr–O1	3.09(1)
<(Mn/Mo)–O>	1.95(1)	Sr–O1	2.57(1)
[Mn/Nb] $_{2c}O_6$ octahedra		Sr–O2	2.81(2)
(Mn/Mo)–O1 (x2)	2.08(2)	Sr–O2	2.58(2)
(Mn/Mo)–O2 (x2)	2.07(1)	Sr–O2	3.10(2)
(Mn/Mo)–O3 (x2)	2.06(1)	Sr–O2	2.82(2)
<(Mn/Mo)–O>	2.07(1)	Sr–O3	2.85(2)
[B] $_{2b}O_1$ –[B] $_{2d}$ (x2)	165.4(6)	Sr–O3	3.04(2)
[B] $_{2b}O_2$ –[B] $_{2d}$ (x2)	165.3(5)	Sr–O3	2.64(2)
[B] $_{2b}O_3$ –[B] $_{2d}$ (x2)	168.0(4)	Sr–O3	2.78(2)
<[B] $_{2b}O$ –[B] $_{2d}$ >	166.2	<Sr–O>	2.740

*Fixed Parameters (see text).

3.2. Thermogravimetric analysis (TGA)

Fig. 3 illustrates the TGA curves in air (oxidation process) of SMM and BMM. The samples are stable in an air flow up to 300 °C; above this temperature, an oxidation process starts. The final products of the oxidation process were identified by XRPD, according the following reactions:

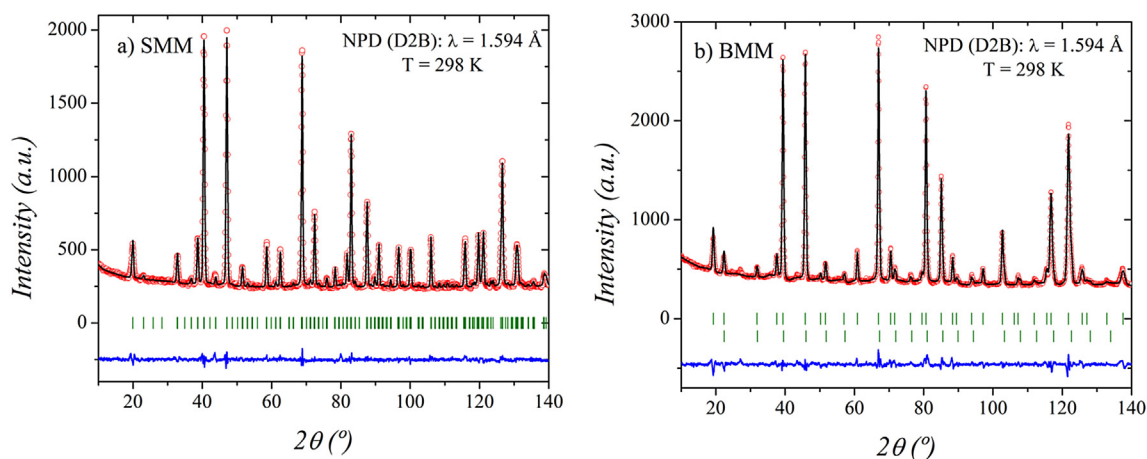
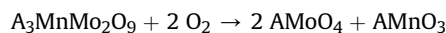


Fig. 2. Observed (circles), calculated (full line) and difference (bottom) Rietveld profiles at room temperature for a) SMM and b) BMM after NPD refinement at RT. In b) the second series of tick marks correspond to the Bragg reflections for the $BaMoO_3$ minor impurity.

Table 2

Crystallographic data for Ba₃MnMo₂O₉ phase from NPD data at RT. Space group: *Fm*3*m*, *Z* = 4. Unit-cell parameters: *a* = *b* = *c* = 8.14900(8) Å, and *V* = 541.145(9) Å³.

a) Positional, displacement and occupancy factors						
Atom	Wyckoff site	<i>x/a</i> β11	<i>y/b</i> β22	<i>z/c</i> β33	B _{iso} /Å ²	Occ
Ba	8c	0.25	0.25	0.25	–	1
		9(1)	9(1)	9(1)		
Mo	4b	1/2	1/2	1/2	–	1
		7(1)	7(1)	7(1)		
Mn	4a	0	0	0	0.3*	0.66
Mo	4a	0	0	0	0.3*	0.33
O	24e	0.2581(2)	0	0	–	1
		13(2)	24(1)	24(1)		

R_p = 2.56%. R_{wp} = 3.31%. R_{exp} = 3.77%. χ² = 1.16 R_{Bragg} = 2.13%

b) Main distances (Å) and angles (°).			
[Mo] _{4b} O ₆ octahedra	BaO ₁₂ polyhedra		
Mo–O (x6)	1.9717(3)	Ba–O	2.8819(2)
[Mn/Mo] _{4a} O ₆ octahedra			
(Mn/Mo)–O (x6)	2.1028(3)		
Mo–O–(Mn/Mo) (x6)	180		

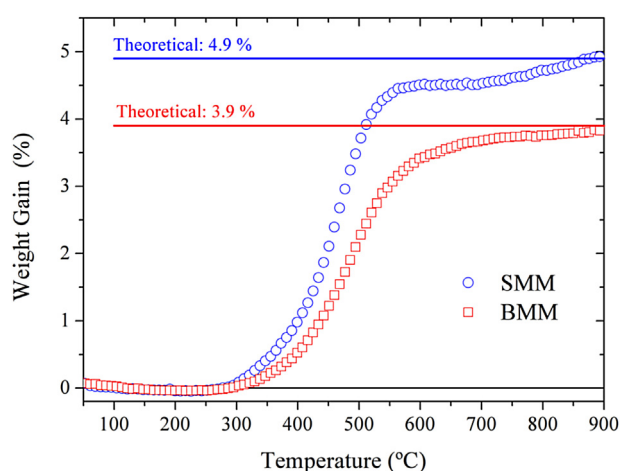


Fig. 3. TGA curves of SMM and BMM samples (oxidation process) obtained in air flow at 5 °C min⁻¹.

The experimental weight gains for these reactions are in agreement with the theoretical ones, 4.9% and 3.9% for SMM and BMM respectively, as can be seen in Fig. 3. These facts indicate that, within the experimental errors, the Mn and Mo ions are either as A₃Mn²⁺Mo⁵⁺₂O₉ or as A₃Mn³⁺Mo^{4.5+}₂O₉, which are not possible to discriminate. This assumption is true considering that the oxygen occupation and the ratio Mn/Mo are 1 and 0.5 respectively. Both facts were confirmed by TGA, XRPD and NPD.

3.3. Magnetic data

The magnetization vs. temperature curves, measured at *H* = 1 kOe, are displayed in Fig. 4a). The samples have a moderate magnetic susceptibility and a splitting between ZFC (zero field cooling) and FC (field cooling) magnetization curves at very low temperature. A more detailed measurement performed at 100 Oe is shown in the inset of Fig. 4a). The splitting between ZFC and FC magnetization is clearly observed below 12 and 9 K for SMM and BMM, respectively.

The magnetization vs. magnetic field curves at 2 K and RT are

plotted in Fig. 4b). In both samples the *M* vs *H* isotherm at 2 K shows significant hysteresis, but saturation is not achieved even at 50 kOe. At *T* = 300 K, a minor ferri or ferromagnetic component is observed only in BMN, see insert in Fig. 4b).

The inverse of susceptibility (Fig. 5) is completely linear above the magnetic-ordering temperature in SMM; however, this is not observed for BMM. SMM presents a paramagnetic like behaviour above 20 K, and a Curie–Weiss fit gives a paramagnetic moment of 4.55 μ_B and a Weiss temperature of –37 K. The negative θ_{Weiss} clearly indicates the predominance of antiferromagnetic interactions. For BMM there is a gradual change in the χ⁻¹ vs. *T* slope, suggesting a minor ferri or ferromagnetic component as observed in the *M* vs *H* loop; the data were fitted with the susceptibility obtained by the mean field theory of ferrimagnetism (MFTF), χ⁻¹ = (*T* – θ)/C_M – ξ/(*T* – θ') [19]. The parameters obtained are C_M = 2.58 Oe mol/emu K; θ = –147 K; θ' = –28842 K and ξ = 667 Oe mol K/emu. The obtained C_M value is similar to that obtained in SMM from the Curie–Weiss fit.

3.4. X-ray absorption spectra

The Mn–K edges of SMM and BMM with the MnO standard compound are shown in Fig. 6. Two more manganese oxides, Mn₂O₃ and MnO₂, were also measured as a reference. The determination of the edge position from the energy at which the absorption is half the total jump will give an estimation of the nominal oxidation state of Mn, compared to these well-known references (MnO, Mn₂O₃ and MnO₂), and whether this oxidation state is localized or fluctuating. The inset of Fig. 6, plotting the chemical shifts of the three standards together with those of SMM and BMM, clearly show that the valence state of Mn in both compounds is divalent (+2.3 for SMM and +2.1 for BMM).

3.5. Electric transport properties (*d.c.* and *a.c.* measurements)

The electrical resistivities (*d.c.*) of SMM and BMM perovskites at room temperature are 150 and 2900 Ω m respectively. Due to the high resistivity of BMM it was not possible to measure its temperature variation. As shown in Fig. 7, for SMM the resistivity increases gradually from 300 to 80 K. The negative slope value of the resistivity vs. temperature curve can be associated with a semiconductor response of the material. The thermal evolution of resistivity can be explained in terms of Mott variable-range hopping (VRH) mechanism [20] in the high temperature range (inset of Fig. 7).

The transport properties also were studied from Impedance Spectroscopy (*a.c.* measurements) in the temperature range of 100–320 K. The impedance diagram (Nyquist plot (–Z'' vs Z')) for SMM and BMM at 300 K, is shown in Fig. 8. The Nyquist plots are not perfect semicircles; this is a well-known feature due to the non-Debye type of relaxation, in which there is a distribution of relaxation times [21]. This non-ideal behaviour can be correlated to several factors, such as grain orientation, grain boundary, stress–strain phenomena and atomic defect distribution. The SMM spectra exhibit two semicircles corresponding to the grain bulk and grain boundary effects. The contribution positioned at low frequencies corresponds to the grain boundary response and, in the high frequency region, the specific property of the bulk appears [21]. In SMM the experimental data were fitted with two R-CPE (resistance in parallel with a phase constant element) elements in series, as shown in the inset of Fig. 8. The assignment of the two semicircular arcs is consistent with the “brick-layer model” for polycrystalline samples [21]. On the other hand, for BMM the experimental data were fitted a single R-CPE element. This behaviour is probably due to the fact that the total resistance is dominated by this grain

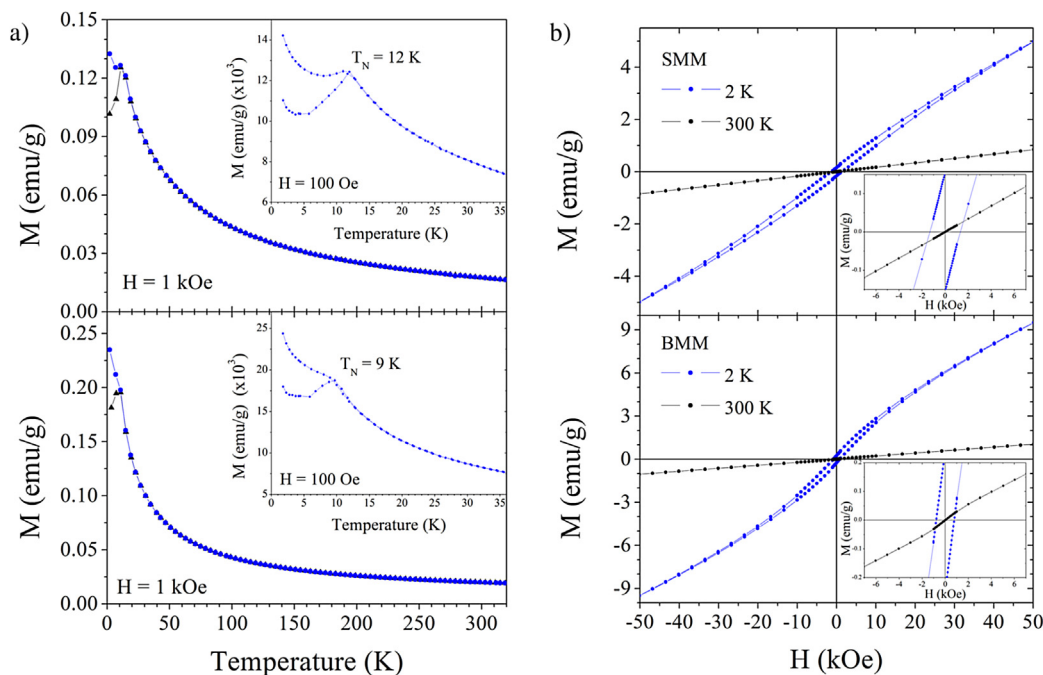


Fig. 4. a) Magnetization as a function of temperature recorded at 1 kOe. The inset shows more detailed magnetization data recorded at 100 Oe below 40 K for SMM (top) and BMM (bottom). b) Magnetization vs. magnetic field isotherms at 2 and 300 K. The inset figure shows a close up of the loops in the low-field region.

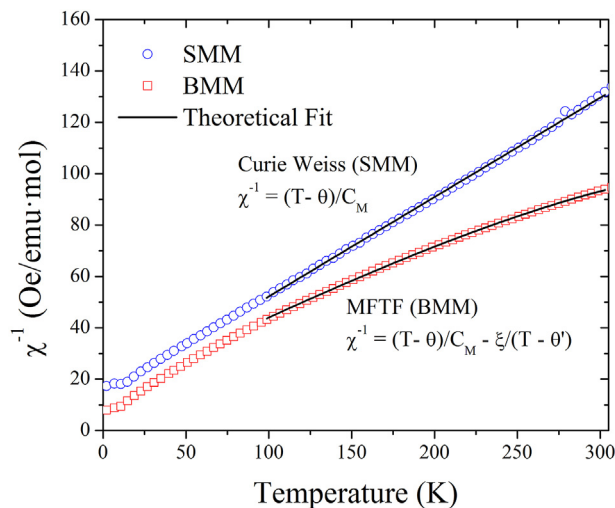


Fig. 5. Inverse of the magnetic susceptibility as a function of temperature for SMM and BMM.

boundary contribution. Alternatively, in the event of very high dielectric constant of the bulk material, both contributions (grain bulk and boundary) could have almost equal relaxation times.

4. Discussion

The perovskite structure ABO_3 can be viewed as a network of corner-sharing BO_6 octahedra, with the A cations occupying the voids formed by these octahedra. If the size of A cations becomes small, the BO_6 octahedra tilt in order to optimize the A-O contacts. $A_3MnMo_2O_9$ adopts this well-known structure, in which $(Mo_{1-2}Mn_2)O_6$ and $(Mo_{1/3+\alpha}Mn_{2/3-\alpha})O_6$ octahedra alternate along the three crystallographic directions. In the present oxides, α is 0.036 and 0 for SMM and BMM, respectively. Both phases are

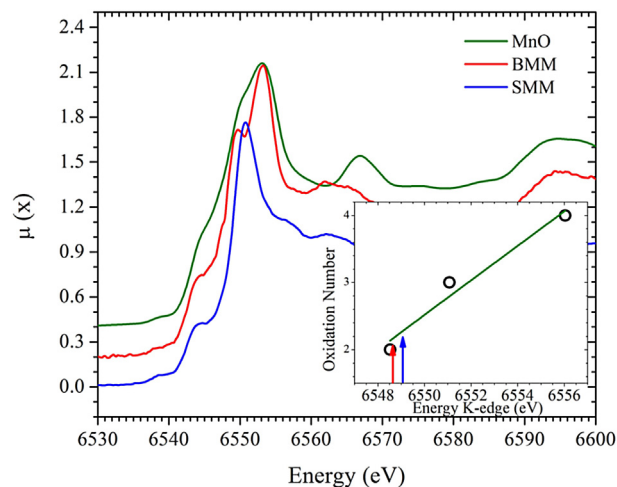


Fig. 6. (colour online) Mn K-edge XANES spectra of SMM, BMM and MnO reference pattern at room temperature. Inset: Oxidation number of Mn as a function of the K-edge energies.

almost fully ordered (within the intrinsic disorder) with a DO = 0.89 and 1.00 for SMN and BMM, respectively.

From the NPD data, the refined crystallographic formulae are $Sr_2[Mn_{0.63(1)}Mo_{0.37(1)}]_2c[Mn_{0.04(1)}Mo_{0.96(1)}]_{4b}O_6$ and $Ba_2[Mn_{0.66-Mo_{0.33}}]_{4a}[Mo]_{4b}O_6$ for SMM and BMM, respectively. The refined site occupancies also show that the oxygen content is close to 1 in both samples. Given the size of Ba^{2+} cations, the octahedral network is not tilted, keeping $B_{4b}-O-B_{4a}$ angles of 180° . However, for $A = Sr^{2+}$, the octahedra are tilted (tilt system: $a^+b^-b^-$) with an average angle of 6.9° , estimated as $\varphi = (180 - \theta)/2$, where $\theta = \langle B'-O-B'' \rangle$.

The reducing conditions (time of treatment, temperature and hydrogen concentrations) were carefully tuned in order to obtain the optimal conditions in the synthesis. For the $A_3MnMo_2O_9$ stoichiometry, we expected oxidation states between $A_3Mn^{2+}Mo^{5+}_2O_9$

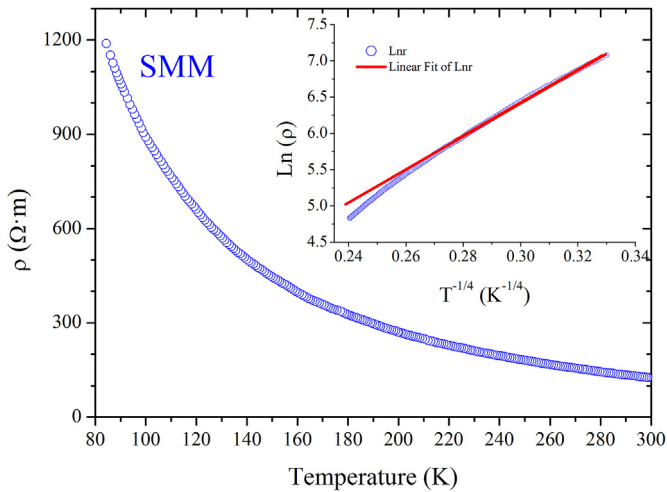


Fig. 7. Electrical resistivity as a function of temperature; the inset shows the linear behaviour in $\ln \rho$ vs. $T^{-1/4}$ plot (VRH theory) for SMM.

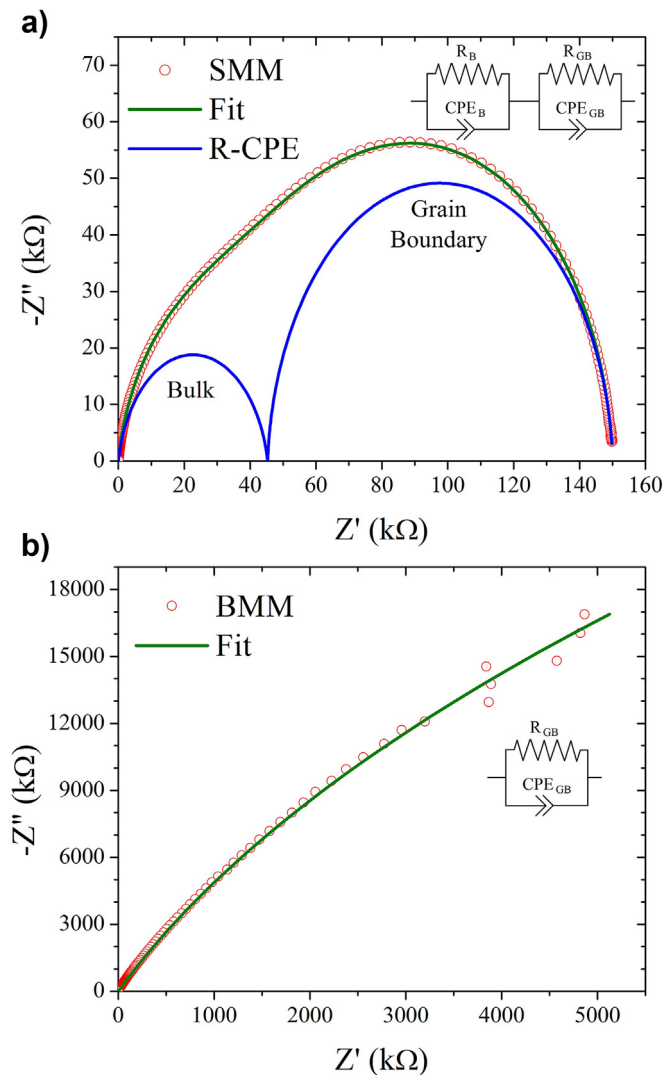


Fig. 8. Impedance spectrum of a) SMM and b) BMM at 300 K. The continuous curves are fits with to the equivalent circuit shown in each figure.

and $A_3Mn^{3+}Mo^{4.5+}_2O_9$, as commented before. This fact was confirmed from TGA analysis. Additionally, from the X-ray absorption spectra could clearly verify that the electronic configuration of manganese is close to $Mn^{2+}(3d^5)$.

In order to confirm the oxidation number of Mo, the average distance $\langle Mo-O \rangle$ of our compounds (determined from accurate NPD data) was compared with those present in other phases with Mo exhibiting oxidation numbers of 4 or 6 such as in $AMoO_3$ or A_2MnMoO_6 , respectively. In Fig. 9 we plot the $\langle Mo-O \rangle$ distances reported by several authors for $AMo^{4+}O_3$ and $A_2MnMo^{6+}O_6$ ($A = Sr$ and Ba) [18,22–28]. Then, we calculate the arithmetic average for respective data in points Mo^{4+} and Mo^{6+} and we draw a linear fit between them. As shown in Fig. 9 the $\langle Mo-O \rangle$ distances for SMM BMM perfectly correspond to those expected for $\langle Mo^{5+}-O \rangle$ bond lengths. This supports that the electronic configuration is $A_3Mn^{2+}Mo^{5+}_2O_9$ in both cases.

The magnetic measurements suggest a magnetic order at low temperatures, below 12 and 9 K for SMM and BMM, respectively. The difference between ZFC and FC curves and the M vs. H plots indicate the presence of different magnetic ground states reached at low temperature. The multiple ground states are a consequence of the microscopic competition between ferromagnetic and anti-ferromagnetic interactions present in the system. These include antiferromagnetic (AFM) $Mn^{2+}-O-Mn^{2+}$ and $Mo^{5+}-O-Mo^{5+}$ and ferromagnetic (FM) $Mn^{2+}-O-Mo^{5+}$ interactions mediated by superexchange. This behaviour, involving low magnetic order temperatures and competing interactions, is observed in other Mn-containing double perovskites with Mn^{2+} as A_2MnBO_6 ($A = Ca, Sr$ and Ba ; $B = W, Mo$ and Te) [25–27,29], as well as perovskites with Mn^{3+} as $(Ca,Sr)_2Mn(Sb,Ta)O_6$ or $Ca_3Mn_2WO_6$ [30,14]. Greater magnetic order temperatures (40 K) were also observed in compounds with mixed valence states $Mn^{3+/4+}$ as $Ca_3Mn_2NbO_9$ [14].

Moreover, SMM obeys the Curie–Weiss law in the paramagnetic region whereas BMM was well modelled by the mean field theory of ferrimagnetism, as shown in Fig. 5. In both cases the obtained magnetic moments are close to $4.55 \mu_B$. These values are lower than the theoretical values for $Mn^{2+}Mo^{5+}$ or $Mn^{3+}Mo^{4+/5+}$ possibilities, which are 5.22 and $4.83 \mu_B$ respectively. These differences may arise from the presence of magnetic interactions in the high temperature region.

Both samples show high resistivity, 150 and 2900 Ω m at room temperature for SMM and BMM, respectively. SMM displays a semiconducting behaviour in all the temperature range (80–300 K), modelled with a VRH mechanism in the following form:

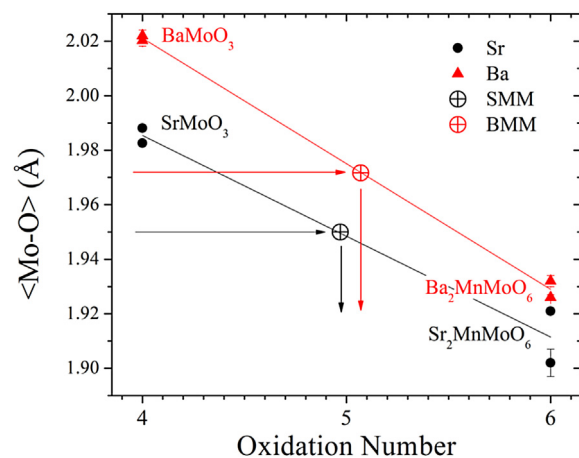


Fig. 9. Evolution of the $\langle Mo-O \rangle$ distances with the oxidation number of Mo from RT NPD data.

$$\rho = \rho_0 \exp(T_0/T)^{-1/4}$$

where T_0 is proportional to $\alpha^3/N(E_F)$, α is the localization length, and $N(E_F)$ is the density of states at the Fermi level [20]. From this fit the T_0 value obtained is 22.8(1) K.

From the impedance spectroscopy the highest resistance was also observed in BMM, while in SMM the grain and grain boundary effects were understood in terms of the brick-layer model. The thermal evolution of resistance parameters (R_B and R_{GB}) obtained from the fit of Nyquist plots shows a VRH mechanism as displayed in Fig. 10. The GB effect exhibits a linear behaviour below 270 K while the bulk conduction (only observed in SMM) is linear in all the temperature range. Besides, the T_0 value for BMM is slightly lower than that for SMM and these, bulk and GB, are similar to those obtained by d.c. measurements.

The transport properties describe both perovskites as Mott insulator materials; this is striking taking into account that similar phases (without Mn) as SrMoO_3 present a metallic state with a total electron delocalization [23]. On the other hand, we can think of BMM and SMM ($\text{Mn}^{2+}(3 d^5)\text{-Mo}^{5+}(4 d^1)$) as isoelectronic materials with the magnetoresistant $\text{Sr}_2\text{FeMoO}_6$ ($\text{Fe}^{3+}(3 d^5)\text{-Mo}^{5+}(4 d^1)$), even with the isostructural $\text{Ba}_3\text{FeMo}_2\text{O}_9$ ($\text{Fe}(3 d^{6-\delta})\text{-Mo}(4 d^{1+\delta/2})$) perovskite with δ close to 1 [7,15]. However, the observed behaviour is substantially different. Considering the similarities and differences, and in the absence of band-structure calculations, we could considerate that the single electron of Mo^{5+} in a 4d-orbital of t_{2g} symmetry is localized, in contrast with SrMoO_3 , $\text{Sr}_2\text{FeMoO}_6$ or $\text{Ba}_3\text{FeMo}_2\text{O}_9$ [23,7,15] where there is an electronic delocalization driving a metallic state. In the same way, there are no mixed valence states in Mn and Mo, as noted previously, since the oxidation states of Mn and Mo are close to +2 and +5, respectively. The absence of mixed valence state in SMM and BMM, account for the transport behaviour in both samples.

5. Conclusions

Two new double perovskites $\text{Sr}_3\text{MnMo}_2\text{O}_9$ and $\text{Ba}_3\text{MnMo}_2\text{O}_9$ with electronic configurations close to $\text{Mn}^{2+}(3 d^5)\text{-Mo}^{5+}(4 d^1)$ have been obtained by a citrate precursor method, followed by an annealing in a H_2/N_2 flow at 1200 °C. The crystal structures were refined from NPD at RT as monoclinic ($P2_1/n$) and cubic ($Fm\bar{3}m$) for SMM and BMM, respectively. The electronic configurations were

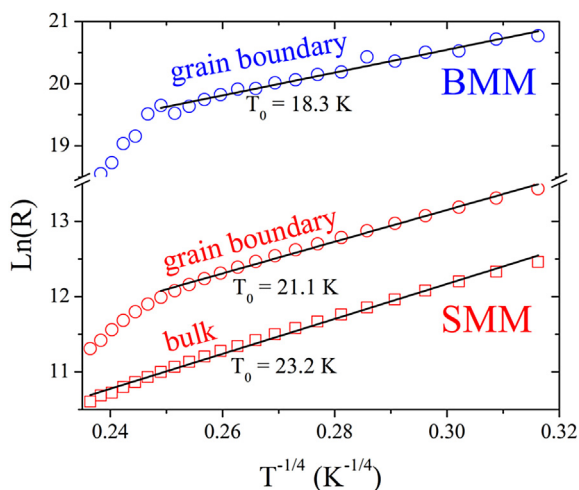


Fig. 10. (colour online) Grain boundary and Bulk resistances vs $T^{-1/4}$. The solid lines correspond to the linear fit of VRH model.

deduced from XANES for Mn ions, and from NPD data for Mo ions in octahedral positions. Both species, Mn^{2+} and Mo^{5+} are compatible in this intrinsically disordered stoichiometry, $\text{A}_3\text{MnMo}_2\text{O}_9$.

Magnetic interactions are observed below 12 and 9 K for SMM and BMM, respectively. While SMM presents a Curie–Weiss behaviour, BMM was modelled by the mean field theory of ferrimagnetism, showing similar Curie constants in both fits. The transport properties display a semiconducting behaviour modelled by a variable-range hopping mechanism either from d.c. or a.c. measurements. This transport behaviour is in accord with the electronic configurations $\text{Mn}(3 d^{5-\delta})\text{-Mo}(4 d^{1+\delta/2})$ when δ value is close to 0, where the 4 d^1 electrons in Mo are localized, accounting for the large resistivities observed in both systems.

Acknowledgements

J.C.P. thanks CONICET (Project PIP 112-200801-01360), SECyT-UNSL (Project PROICO 2-7707- 22/Q823) and ANPCYT (Project PICT 6/25459). R.D.S. thanks UN Cuyo, CONICET and ANPCyT (Argentina) under grants 06/C389, PIP-490 and PICT2007-0832/PICT2011-0752. C.A.L., M.E.S., J.C.P. and R.D.S. are members of CONICET. J.A.A. acknowledges the financial support of the Spanish Please provide the grant number for: 1) Ministry of Education, 2) Brazilian Synchrotron Light Laboratory, if any. Ministry of Education to the project MAT2013-41099-R. We are grateful to ILL for making all facilities available. Also, the authors thank the Brazilian Synchrotron Light Laboratory (LNLS) for the beamtime (D04B - XAFS1-11681), and the staff of the XAFS1 Beamline for providing assistance during the experiment.

References

- [1] C.N.R. Rao, B. Raveau, Transition Metal Oxides: Structure, Properties, and Synthesis of Ceramic Oxides, John Wiley & Sons, New York, 1998.
- [2] D.A. Bonn, Review, Nat. Phys. 2 (2006) 159–168.
- [3] J. Alonso, Chem. Phys. Chem. 11 (2010) 58–60.
- [4] Y.H. Huang, R.I. Dass, Z.L. Xing, J.B. Goodenough, Science 5771 (2006) 254–257.
- [5] C. Sun, U. Stimming, J. Power Sources 171 (2007) 247–260.
- [6] B. Raveau, Prog. Solid State Chem. 35 (2007) 171–173.
- [7] K.-I. Kobayashi, T. Kimura, H. Sawada, K. Terakura, Y. Tokura, Nature 395 (1998) 677–680.
- [8] T.H. Kim, M. Uehara, S.-W. Cheong, S. Lee, Appl. Phys. Lett. 74 (1999) 1737–1739.
- [9] M.C. Viola, J.A. Alonso, J.C. Pedregosa, R.E. Carbonio, Eur. J. Inorg. Chem. (2005) 1559–1564.
- [10] M. Retuerto, J.A. Alonso, M.J. Martínez-Lope, M. García-Hernández, C.A. López, M.C. Viola, J.C. Pedregosa, M.T. Fernández-Díaz, Eur. J. Inorg. Chem. (2009) 3750–3757.
- [11] R.M. Pinacca, M.C. Viola, J.C. Pedregosa, R.E. Carbonio, J.A. Alonso, J. Mater. Chem. 15 (2005) 4648–4653.
- [12] M.S. Augsburger, M.C. Viola, J.C. Pedregosa, R.E. Carbonio, J.A. Alonso, J. Mater. Chem. 16 (2006) 4235–4242.
- [13] C.A. López, M.C. Viola, J.C. Pedregosa, J.A. Alonso, M.T. Fernández-Díaz, Eur. J. Inorg. Chem. (2010) 4110–4120.
- [14] C.A. López, M.E. Saleta, J.C. Pedregosa, R.D. Sánchez, J.A. Alonso, M.T. Fernández-Díaz, J. Solid State Chem. 210 (2013) 1–9.
- [15] C.A. López, M.E. Saleta, J.C. Pedregosa, R.D. Sánchez, J.A. Alonso, M.T. Fernández-Díaz, Eur. J. Inorg. Chem. (2014) 3555–3563.
- [16] H.M. Rietveld, J. Appl. Crystallogr. 2 (1969) 65–71.
- [17] J. Rodríguez-Carvajal, Phys. B 192 (1993) 55–69.
- [18] V. Nassif, R.E. Carbonio, J.A. Alonso, J. Solid State Chem. 146 (1999) 266–270.
- [19] J.S. Smart, Effective Field Theories of Magnetism, Saunders Company, W.B., 1966.
- [20] N.F. Mott, Conduction in Non-crystalline Materials, Clarendon Press, Oxford, 1993.
- [21] J. Ross Macdonald, Impedance Spectroscopy Theory, Experiment, and Applications, second ed., John Wiley & Sons, 2005.
- [22] L.H. Brixner, J. Inorg. Nucl. Chem. 14 (1960) 225–230.
- [23] R.B. Macquart, B.J. Kennedy, M. Avdeev, J. Solid State Chem. 183 (2010) 249–254.
- [24] P. Xiao, X. Ge, Z. Liu, J. Wang, X. Wang, J. Alloy Compd. 587 (2014) 326–331.
- [25] A.K. Azad, S.-G. Eriksson, S.A. Ivanov, R. Mathieu, P. Svedlindh, J. Eriksen, H. Rundlöf, J. Alloys Compd. 364 (2004) 77–82.
- [26] M.J. Martínez-Lope, J.A. Alonso, M.T. Casais, Z. Naturforsch 58b (2003)

- 571–576.
- [27] A. Muñoz, J.A. Alonso, M.T. Casais, M.J. Martínez-Lope, M.T. Fernández-Díaz, *J. Phys. Condens. Matter* 14 (2002) 8817–8830.
- [28] K. Zheng, K. Swierczek, *J. Eur. Cer. Soc.* 34 (2014) 4273–4284.
- [29] L. Ortega-San Martín, J.P. Chapman, L. Lezama, J. Sánchez Marcos, J. Rodríguez-Fernández, M.I. Arriortua, T. Rojo, *Eur. J. Inorg. Chem.* (2006) 1362–1370.
- [30] T. Kumar Mandal, V.V. Poltavets, M. Croft, M. Greenblatt, *J. Solid State Chem.* 181 (2008) 2325–2331.